

Full length article

Diffusion mechanisms of C in 100, 110 and 111 Fe surfaces studied using kinetic activation-relaxation technique



Oscar A. Restrepo^{a, d, *}, Charlotte S. Becquart^b, Fedwa El-Mellouhi^c, Othmane Bouhali^d, Normand Mousseau^a

^a Département de Physique and Regroupement Québécois sur Les Matériaux de Pointe, Université de Montréal, Case Postale 6128, Succursale Centre-ville, Montréal, QC H3C 3J7, Canada

^b Univ. Lille, CNRS, INRA, ENSCL, UMR 8207, UMET, Unité Matériaux et Transformations, F 59 000 Lille, France

^c Qatar Environment and Energy Research Institute, Hamad Bin Khalifa University, PoBox 3411, Doha, Qatar

^d Texas A&M University at Qatar, Doha, Qatar

ARTICLE INFO

Article history:

Received 3 February 2017

Received in revised form

4 July 2017

Accepted 4 July 2017

Available online 7 July 2017

Keywords:

KMC

MD

Fe-C

Surface diffusion

Migration energy

ABSTRACT

The physics of Fe-C surface interactions is of fundamental importance to phenomena such as corrosion, catalysis, synthesis of graphene, new steels, etc. To better understand this question, we perform an extensive characterization of the energy landscape for carbon diffusion from bulk to surfaces for bcc iron at low C concentration. C diffusion mechanisms over the three main Fe-surfaces – (100), (110) and (111) – are studied computationally using the kinetic activation-relaxation technique (k-ART), an off-lattice kinetic Monte Carlo algorithm. Migration and adsorption energies on surfaces as well as absorption energies into the subsurfaces are predicted and then compared to density functional theory (DFT) and experiment. The energy landscape along C-diffusion pathways from bulk to surface is constructed allowing a more extensive characterization of the diffusion pathways between surface and subsurface. In particular, effective migration energies from (100), (110) and (111) surfaces, to the bulk octahedral site are found to be around ~1.6 eV, ~1.2 eV and ~1.3 eV respectively suggesting that C insertion into the bulk cannot take place in pure crystalline Fe, irrespective of the exposed surface.

© 2017 Acta Materialia Inc. Published by Elsevier Ltd. All rights reserved.

1. Introduction

Carbon interaction with iron surfaces is associated with several processes such as steel fabrication, metal dusting corrosion [1], iron-based catalyst used in Fisher-Tropsch synthesis [2], design of new materials for fission reactors [3], and synthesis of high-quality graphene sheets and carbon nanotubes [4–6]. In spite of considerable experimental and computational efforts [7–10], atomistic details regarding the carbon surface diffusion as well as adsorption, absorption, insertion and segregation pathways are still lacking. For instance, it is known that the mechanisms by which catastrophic metal dusting corrosion in steels happens can be generally explained in three steps: first, the formation of a cementite layer at the metal surface; followed by, cementite decomposition that leads

to graphite nucleation; and in a final step, the precipitation of iron particles in the coke which acts as catalyst for additional graphite deposition [11]. However, the exact atomistic mechanisms are not well understood. Similarly, in Fisher-Tropsch synthesis C deposition and diffusion is undesirable because the metal catalytic activity can be reduced [12]. Therefore, an explicit understanding of the mechanisms of diffusion could help to solve this problem.

In recent years, carbon interaction with iron surfaces has also been linked to fashionable applications, contributing to reviving the interest in these fundamentals problems. For example, Vinogradov et al. [4] performed *in situ* epitaxial graphene growth on (110) Fe-surface using chemical vapor deposition (CVD) at relatively low temperatures. This graphene monolayer exhibited a novel periodically corrugated pattern on (110) Fe-surface, and was obtained by going beyond the thermodynamic equilibrium conditions during the CVD process to avoid formation of carbide phases.

Several experimental and theoretical studies made predictions regarding C migration energies on and through Fe-surfaces [6–10,12]. Adsorption and segregation of carbon atoms on (100)

* Corresponding author. Département de Physique and Regroupement Québécois sur Les Matériaux de Pointe, Université de Montréal, Case Postale 6128, Succursale Centre-ville, Montréal, QC H3C 3J7, Canada.

E-mail address: ores77@gmail.com (O.A. Restrepo).

Fe-surface, for instance, has been studied using low-energy electron diffraction [13,14]. Similarly, C segregation, carbide formation and graphite formation at higher coverage have been observed on (111) Fe-surface [15,16], although details are still lacking. On the computational side, studies use static energy calculations with either density-functional theory (DFT) or empirical potential models, generally coupled with tools such as nudge elastic band method (NEB) [17,18] to refine the diffusion pathway. For instance, Jiang and Carter did DFT studies of C adsorption and diffusion in Fe (100) and (110) surfaces at a coverage of 0.25 monolayers (ML) [10]. Later, Riikonen et al. repeated the DFT study at different C concentrations and added diffusion pathways on the (111) Fe-surface [6], finding good agreement with Jiang and Carter. A recent DFT work, however, indicates significant finite size-effects affecting the height of the calculated energy barriers [19,20] suggesting that this issue needs to be revisited using sufficiently large simulation boxes. Furthermore, DFT predicts that C atoms bind strongly to (100) and (110) Fe-surfaces, while the interaction with the (111) Fe-surface is weaker [6]. It also predicts a large barrier of surface diffusion on (100) (due to the stronger bonding between C and the surface), and a less significant barrier for diffusion through the (111) subsurface, thanks to the hollow sites easing the C diffusion to subsurface. It is also well known from DFT that C prefers high coordination sites [6,10], i.e., instead of the three-fold (TF) site C prefers the hollow (H) on the (100) surface while for (110) surface, the long-bridge (LB) site is preferred.

An extensive characterization of the possible diffusion pathways of C adsorbed on various Fe-surfaces either on the surface or towards the bulk of iron is still missing. Such a work would provide a complete picture of the various diffusion mechanisms and evaluate the possible richness of the energy landscape associated with this phenomenon. To achieve this goal, we employ the kinetic activation-relaxation technique (k-ART) [21–24], coupled with a reliable and well-tested C–Fe embedded-atom method (EAM) empirical potential [25,26].

Using this approach, we characterize the energy landscape of a C atom diffusing from bulk bcc-Fe on and through (100), (110) and (111) Fe-surfaces. Following the evolution of the energy landscape over timescales ranging from tenths of microseconds to milliseconds, we generate a detailed picture of the various mechanisms that are subsequently compared to DFT and experimental results published so far.

2. Methodology

2.1. Overview of k-ART

We use the k-ART coupled with the Ackland-Mendelev-Becquart embedded atom method (EAM) potential for Fe–C interactions for the characterization of the C-diffusion on and through three main Fe-surfaces namely (100), (110) and (111). K-ART is an off-lattice on-the-fly kinetic Monte-Carlo (KMC) algorithm with topological classification developed to explore the energy landscape and long-time kinetics of complex systems at the atomic scale, fully including long-range elastic events and disordered environments [21,27,28].

While a detailed description of k-ART can be found in Refs. [21,27,28], we provide here a brief overview of the method. K-ART uses a topological characterization of the local environment surrounding each atom to classify configurations. At the beginning of each KMC step, the local environment surrounding each atom is evaluated using a topological approach. Local graphs are constructed by connecting a list of atoms enclosed in a sphere of 6 Å surrounding the chosen atom with being generated between each atom and their neighbors distant by at most 2.7 Å. These graphs are then analyzed with the NAUTY code [29,30], that returns the

automorphic class associated with the graph and the correspondence with a reference graph.

The algorithm proceeds as follows. (1) After an event, the local topology of atoms involved in the event is computed. (2) If the topology is known, events associated with it are inserted in an active list; if the topology is new, event searches are launched using the activation-relaxation technique (ART nouveau), an open-ended method, to identify diffusion mechanisms and energy barriers [31–33]. (3) A first classification of the active events is generated, with events ordered by their rate, computed as $r_i = \nu e^{E_b/k_B T}$ where, ν , is a prefactor or constant attempt frequency set to 10^{13} s^{-1} , k_B the Boltzmann's constant, T the temperature and $E_b = E_{\text{sad}} - E_{\text{min}}$, is the activation energy for an event defined as the energy difference between the initial minimum E_{min} and the saddle E_{sad} (i.e., the barrier crossed between two adjacent minima). (4) All events with an occurrence probability of 1 in 10 000 or higher are fully reconstructed and relaxed, using ART nouveau, to ensure that elastic and local deformation effects are exactly taken into account [28]. (5) Incorporating these updated barriers in the event list, a time step is drawn from a Poisson distribution, $\Delta t = -\log(\mu) / \sum r_i$, where μ is a random number in (0,1), and an event is selected at random with a weight proportional to its rate, according to standard KMC [24]. (6) After the time is brought forward and the event applied, a new step can be launched, starting at (1). As discussed in Refs. [21,28], atoms characterized by the same automorphic class share the same event lists, allowing k-ART to be applied to a range of environments, from bulk to surface and crystalline to amorphous materials.

2.2. Handling flickering states

Flickering states are states of similar energy separated by low-energy barriers that can dominate event-based KMC simulations and slow system evolution to a halt. To avoid being trapped by these states, k-ART incorporates the basin-auto constructing mean rate method (bac-MRM), which computes an on-the-fly statistically correct analytic solution of the system's average residence time in the connected region of flickering states and of its escape rate as the energy landscape is explored [28,34]. Since the kinetics between states of similar energy separated by a barrier below the basin threshold is resolved statistically, no specific pathway is available for the in-basin motion. To fully characterize kinetics at all relevant timescales, we therefore proceed by slowly raising the basin threshold. We start all simulations with a low basin factor of 0.1 eV and we increase it as flickers appear. For example, for the (100) surface no flickering state is found while for (110), we increase the basin factor to 0.2 eV because of flickers with barriers of 0.11 eV, 0.06 eV and 0.13 eV. The (111) surface is rich with flickers and, therefore, the basin factor is increased up to 0.60 eV after full characterization of the landscape (even with a basin factor of 0.50 eV, the system remains trapped with a basin barrier of 0.57 eV and an inverse barrier of 0.11 eV).

2.3. Force-field

In order to access sufficient length and time scales, we employ an empirical force-field to describe the system. The Fe–Fe interactions are handled by the Embedded Atom Method (EAM) interatomic potential developed by Ackland and Mendelev [35] while the Fe–C interaction part was developed by Becquart and collaborators [25,26]. The combined potential provides a good agreement with DFT calculations in bulk systems [36]. For example, the Fe–C potential has been used with success over different systems for the computation of different properties like the formation of carbon Cottrell atmospheres in bcc-iron [37] and the elastic constants of the martensite [38], as well as model the effect of the

stress field of an edge dislocation on carbon diffusion [39]. This EAM potential is linked to k-ART package through the LAMMPS library, which is used as the force-calculation engine [40,41].

2.4. Samples used

The simulated systems consist of three bcc-Fe slabs with a lattice constant of 2.855 Å and (100), (110) and (111) surfaces oriented along the x axis. Periodic boundary conditions are applied in all directions except along x , which is kept normal to the surface of interest. The first slab, Fe (100), has a surface area of $22.843 \times 22.846 \text{ \AA}^2$ and counts 1024 Fe-atoms and 16 layers; the second, Fe (110), a surface area of $20.188 \times 14.275 \text{ \AA}^2$ with 1300 Fe-atoms and 26 layers; the last, Fe (111), has a surface area of $24.228 \times 20.982 \text{ \AA}^2$ for 1080 Fe-atoms and 30 layers.

2.5. Thermal effects

For all simulations, the temperature is set to 600 K. This value corresponds to the onset temperature for phenomena such as corrosion [7,11]. The choice of temperature does not affect C diffusion in the bulk, which is associated with a single mechanism. However, the specific diffusion pathways at surfaces, where many mechanisms are found, might be affected. Nevertheless, the energy landscape is not affected by temperature, and the general analysis is applicable for conditions away from melting.

2.6. Data analysis

The square displacement is computed according to $SD(t_n) = \sum_{i=1}^N (\mathbf{x}_i(t_n) - \mathbf{x}_i(0))^2$, where N is the number of particles and $\mathbf{x}_i(t_n)$ is the position atom i at KMC step n and time t_n . The diffusion coefficient over a total of M steps can be computed using

Einstein's formula $D = \left(\frac{1}{6t_n^2} \right) \sum_{n=1}^M SD(t_n) \Delta t_n$, where a time average

is considered according to the ergodic hypothesis (We consider 3D diffusion as 2D and 3D diffusion show the same time relation and differ only by a small constant in the prefactor. Since uncertainties in the diffusion due the statistics (limited number of steps) and the choice of a fixed prefactor are much larger than this 4/6 factor). Also, D is computed after the C atom reaches the surface. In bulk, with the prefactor mentioned above, k-ART predicts an approximated C diffusion coefficient of $D \sim 4.8 \times 10^{-14} \text{ m}^2/\text{s}$.

2.7. Geometry and events summarized from DFT literature

The diffusion pathway of a single C atom in a perfect crystal is rather simple [26,42]: as shown in Fig. 1, the C atom jumps between octahedral sites (OS) via a transition state located in the middle of the pathway, in a tetrahedral site (s), with a 0.815 eV barrier, in agreement with DFT calculations [36]. Similarly, according to DFT [6,10], the C diffusion pathways over the three main surfaces are also simple: diffusion from a stable site to another stable site happens in one step over (100) and (110) and in two steps or more over the (111) surface, as predicted in Refs. [6,10].

According to DFT calculations, C atoms at surfaces are expected to adsorb at sites of maximum coordination, i.e., those sites with a maximum number of Fe neighbors— i.e. hollow (H), long bridge (LB) and quasi four fold (GS) on (100), (110) and (111) surfaces, respectively [6,10]. In Fig. 1, we observe that the number of symmetric events from each one of these high-coordination sites (i.e. events having the same barrier associated but going to a symmetrically equivalent direction) is four for the bulk and for both (100) and (110) surfaces. On the (111) surface, we observe six possible

events: four are from the GS site (see for example, from the GS position at the center of the cell, two jumps to symmetrical positions A plus two jumps to symmetrical positions GS at right) and the other two are from A to GS symmetrical positions at left and right. Using these states a simple catalog can be constructed.

In what follows, and to facilitate comparison, we use the notation of Jiang and Carter [10] to label the various geometrical points that are presented in Fig. 1 for the bulk and (100) and (110) surfaces; for (111) surface, we use our own notation as Jiang and Carter did not study this surface.

3. Results and discussion

In the simulations presented here, ART events are centered on C atoms only, leaving aside the Fe motion in the bulk or at the surface. This allows us to better focus on the mechanisms of interest, without affecting the C-related kinetics. With this approach, Fe atoms can move, but in relation with a C-diffusion jump only. We now provide a more detailed characterization of the kinetics observed for each of the three surfaces.

3.1. Diffusion from bulk to the (100) Fe-surface

Fig. 2 shows the geometries and the diffusion mechanisms related to the (100) Fe-surface as well as the diffusion pathways and energy landscape computed with k-ART. More precisely, Fig. 2a shows a superposition of the all C minima visited during the KMC simulation. These points correspond to the adsorption sites most visited on the (100) surface. Fig. 2b shows the diffusion mechanisms from the subsurface to the surface and across the surface, and panel c, d and e present the evolution of the respective minimum and saddle energies over three different representative intervals.

The k-ART simulations identify two local metastable minima located at bridge position B (on the surface) and B' (situated 0.92 Å above the surface), as seen Fig. 2b and d. K-ART finds therefore two pathways connecting H sites. The first path, through B, involves a first barrier at 0.80 eV while the second pathway goes through a 1.04 eV barrier into B'. With a 0.03 eV barrier to get into a new H site, B' lifetime is only 60 fs at 600 K, resulting in an effective single-step pathway connecting H sites. Nevertheless, with an energy difference of 0.24 eV between the pathway's barriers, the first path, going through B, occurs most of the times, as going through B' occurs only in 1.0% of all KMC steps at 600 K. This picture is consistent with results from DFT for the (100) surface, that predict motion between two hollow sites in one step with a transition state (saddle) located at the bridge (B) site but a larger barrier of 1.3 eV [10] compared to the EAM barrier of 0.80 eV and 1.04 eV. Although the environment around the B site is rougher with the EAM, the overall pathway corresponds to the saddle geometrical position predicted by DFT. DFT pathways are typically generated from pre-built trajectories using for instance the NEB. This may explain why the B' site has not been observed with *ab initio* techniques.

Fig. 2c shows the energy landscape for diffusion from the bulk to the surface: during steps 208–210, the C atom moves from a OS₁ state (at 0.81 eV located into the second layer) to state B (at 0.56 eV on surface) by crossing a small barrier of 0.35 eV and from it to the ground state H with a smaller barrier of 0.25 eV. Surface to subsurface diffusion can be understood by following the same energy landscape while reverting the pathways. In this case, an effective reverse barrier of 1.16 eV is computed by moving backward from H to OS₁, i.e. from steps 210 to 208 (this is also observed in Fig. 2e at step 7704). Including the jump from the second layer to OS₂ to the bulk, an effective reverse barrier of 1.63 eV needs to be crossed for inserting a C atom from the (100) surface to the bulk according to our results. This insertion is very improbable because of the high

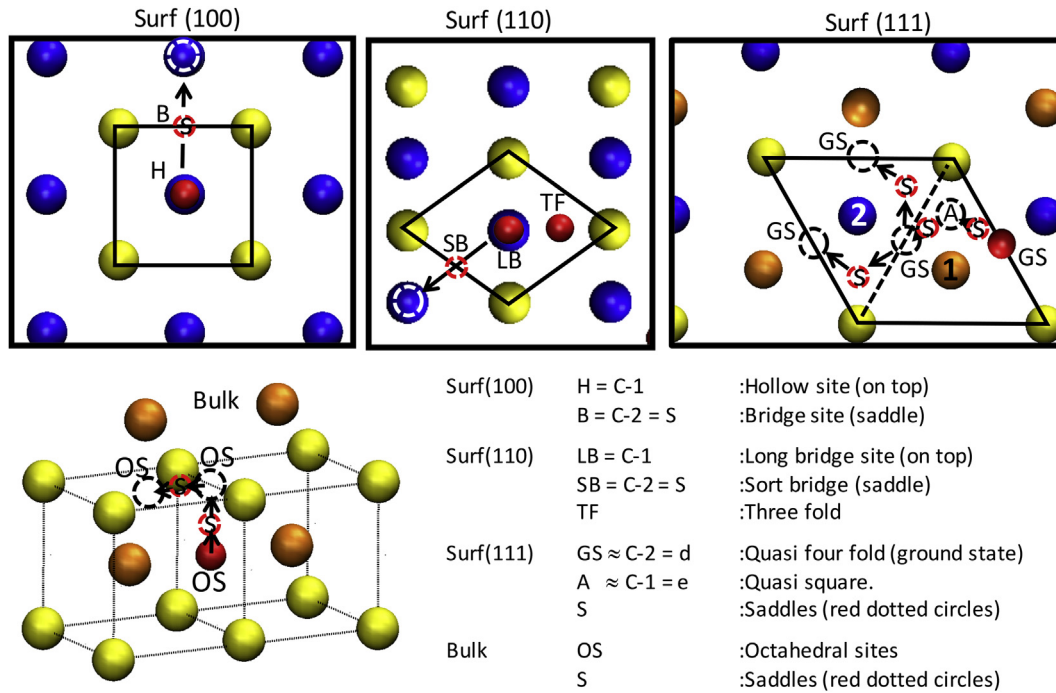


Fig. 1. Top: views of C diffusion pathways as predicted by DFT [10,12] on the three main surfaces; the C atom (in red) jumps to dotted circles via saddle points (s) shown as small red dotted circles. Fe atoms are represented by yellow spheres in the first layer, blue in the second layer and orange in the third layer. Bottom left: a path in bulk Fe. The orange spheres are Fe atoms at the center of the cell. Bottom right: equivalency table between various notations found in the literature: C-1 and C-2 is the notation used by Riikonen et al. [6]; H, B, LB, SB, TF is used by Jian & Carter [10]. On the (111) surface, e, d is the notation used by Liu Xing-wu et al. [12] and GS and A is our notation for similar points. Note that some of the points are near and not perfect equivalents. (For interpretation of the references to colour in this figure legend, the reader is referred to the web version of this article.)

asymmetry: while the jump from the OS_1 to OS_2 state requires crossing a 0.82 eV barrier, the inverse pathways involves a much lower 0.35 eV barrier; as is shown in Fig. 2e.

A comparison of the barriers and inverse barriers energies computed with k-ART-EAM and *ab initio* results found in the literature for the (100) system is presented in Table 1 while Table 2 provides the C atom distances to the surface for the different possible configurations found in this work. Exact comparison to DFT is difficult because most authors only give relative bond distances or even only the layer separation. Nevertheless, when comparison is possible, the EAM potential matches the DFT results relatively well.

Now that the atomic mechanisms of diffusion over the (100) surface have been clarified, we can analyze their relation to effective diffusion. Fig. 3 shows the total square displacement, SD , for the (100) surface as well as the partial square displacements SD_x , SD_y and SD_z for C diffusion along x , y and z directions and the barriers selected at each time step. The displacement is isotropic over the (100) surface as can be inferred from the geometry of the surface. The diffusion coefficient over the (100) surface computed using Einstein's formula is $D \approx 2 \times 10^{-14} \text{ m}^2/\text{s}$, which is of the same order as in the bulk. Over the surface the four energy barriers (blue crosses) are always chosen by sets of two: (0.80, 0.25) eV for the first path and (1.04, 0.03) eV for the second path, in agreement with plots in Fig. 2d and e.

Over a total of 9381 KMC steps, a diffusion time of 663 μs has been obtained with an average time step of 0.07 μs . Activation barriers for the individual jumps encountered in surface-subsurface diffusion are also given in Table 1.

3.2. Diffusion from bulk to the (110) Fe-surface

Surface diffusion mechanisms and their relation to the energy

landscape for the (110) surface system are shown in Fig. 4. In (a), we present a superposition of all the minima visited after the C atom reaches the (110) surface. They correspond to the high-symmetry adsorption sites. Of the three Fe surfaces investigated in this work, the (110) surface has the greatest similarity with planes found in fcc structures, a similarity that makes it an ideal surface for the growth of a graphene layer [4]. This advantage is enhanced by the partial match of the surface with graphene and a Fe–Fe distance close to the graphene lattice constant of 2.48 Å. Not surprisingly, such growth has been observed experimentally in corrosion as well as in practical applications for graphene production [4].

In Fig. 4b we present details of the diffusion mechanisms from the bulk to the (110) surface, with the corresponding minimum and saddle energies shown in Fig. 4c. The diffusion from the bulk (second layer) to the surface goes as follows: from an octahedral site, OS_2 , in second layer at 2.09 Å beneath the surface, the C atom jumps to an OS_1 positioned between the first and second layer at 0.90 Å beneath the surface, with a reduced barrier of 0.75 eV. At this position the C atom pushes the Fe atom 0.58 Å out of the surface (orange dotted circle), in agreement with the 0.50 Å predicted by DFT [10]. From this site, the C atom moves to position A, at 0.26 Å above the top layer and 0.14 eV above ground state by crossing a 0.66 eV barrier (saddle point at S_2). From A, the C atom can then reach the ground state LB at 0.78 Å above the surface, overcoming a small 0.04 eV barrier.

As observed in Fig. 4b,d, surface diffusion takes place with the C atom jumping from the LB site to any of the two threefold positions, TF, and from TF to TF in any other neighbor unit cell. This is done in two or more steps by crossing an effective barrier of 0.58 eV via an intermediate step at position A (see Fig. 4d) and the saddle position S_1 . The two TF states symmetric to A in the same cell are separated by a barrier of 0.06 eV and the barrier from TF to A is 0.13 eV. As

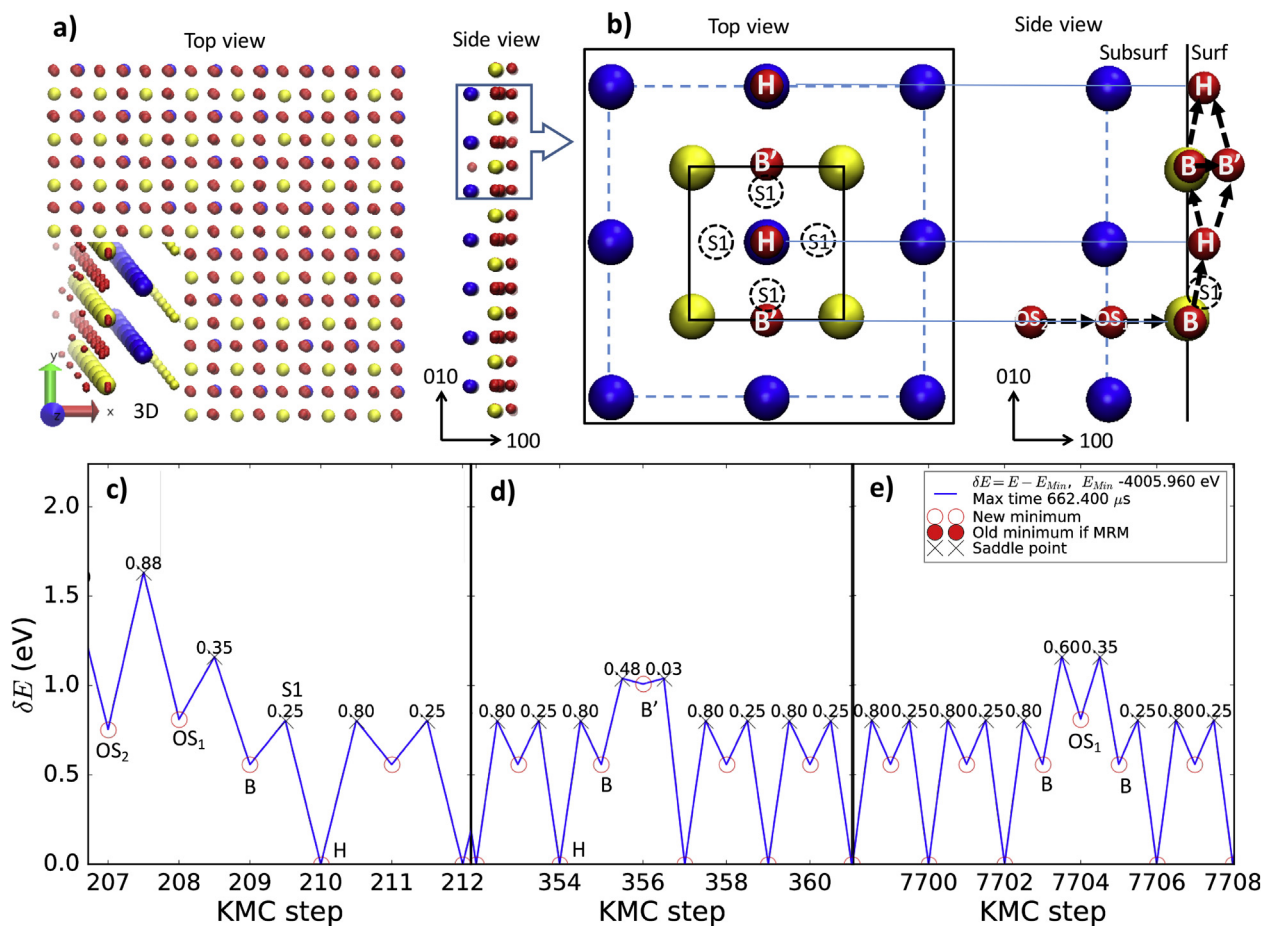


Fig. 2. a) Top and lateral views of the all C positions visited on the Fe (100) surface and subsurface. Red spheres represent the C atom, yellow spheres represent Fe in the first layer and blue spheres, Fe in the second layer. The C positions are marked as: octahedral site OS, hollow H, and bridge positions B and B'. Bottom panels: Energy at the local minima and connecting saddle points as a function of KMC steps. Minimum and saddle energies are given over 3 intervals corresponding to: c) jumps from the bulk to the subsurface; d) jumps on the surface; e) jump from the surface back to the subsurface. $\delta E = E - E_{GS}$, where EGS is the lowest energy found in the simulation. (For interpretation of the references to colour in this figure legend, the reader is referred to the web version of this article.)

mentioned before, the states in which bac-MRM is used produce a discontinuity because the dynamics is lost. This discontinuity is marked with a red dot in Fig. 4d, which indicates that the minimum from the previous step is not the same as the one from which the C arrives to the present KMC step.

Diffusion from the surface to the bulk beyond the second layer has not been observed during the k-ART simulations. However, the C atom visited a few times the OS₁ position between first and second layer by crossing an effective barrier of 1.03 eV from H. This is expected as the barrier to move from A to OS₁ is 0.99 eV versus 0.13 eV to move back to the LB site on the surface. If the C atom jumps to OS₁, the barrier to go deeper into bulk to OS₂ is 0.85 eV versus 0.66 eV to go back to A. With an energy asymmetry of 0.4 eV between the surface LB and the OS closest to the surface, the total barrier needed to be crossed for the C atom to move from the surface LB to bulk, beyond the second layer, is therefore about 1.25 eV. Such an energy can be associated with a timescale of 0.01 s, which is about 50 times longer than our simulation. A summary and comparison of barrier and inverse barrier energies to DFT and to experiment for the (110) system are found in Table 1. Distances of C atomic positions to the (110) Fe surface are found in Table 2.

The total and partial square displacements as well as the energy barrier distribution for C diffusion from bulk to the (110) surface are shown in Fig. 5. The C atom reaches the surface after 32.4 μ s at KMC step 692. Dominated by a 0.58 eV barrier, surface diffusion is much

more rapid as indicated by the KMC simulation: after an additional 5000 steps, the simulations end with a total time of 38.5 μ s leading to a surface diffusion coefficient of $D \approx 8 \times 10^{-13}$ m²/s, approximately one order of magnitude larger than for bulk.

3.3. Diffusion over the (111) surface

The (111) Fe-surface is the most complex of the three studied here. While its topology is simple, its low density provides many metastable sites for C adatoms. Fig. 6 shows the unitary cell (divided in two triangles (1) and (2)) and all the minima found with their symmetries. GS is the ground state, A and A' are local minima 0.13 eV and 0.74 eV above GS, while B, B' and B'' are 0.31 eV, 0.36 eV and 0.80 eV above GS respectively. These states are associated with a number of low-energy barriers leading to flickers, i.e. pathways that do not evolve the system. For example, in the case of the metastable flickering states in triangle (1), A and B are separated by a barrier and reverse barrier of 0.18 [0.09] eV. Now, A is separated from the GS by a barrier and inverse barrier of 0.40 [0.13] eV and B by 0.44 [0.13] eV, respectively. Most of the time, therefore, the C atom will hop between these states, without leaving the cell.

To have an effective diffusion on the (111) surface, the C atom has to cross from one triangle (1) to another triangle (1) by passing via A' in triangle (2) (0.61 Å over the surface) with a barrier of 0.82 eV. Three full possible paths are shown in Fig. 7. Another two

Table 1
Barriers (eV) for C atom diffusion on the (100) (110) and (111) surfaces as well as from the surface to the subsurface: k-ART-EAM, DFT literature and experimental data. Inverse barriers for the reverse processes are given in square brackets. Barriers in parenthesis are measured from the second excited state. The * corresponds to a measure of an effective barrier over the full path to move C to a neighbor cell.

Plane	Path	EAM	Path	DFT	Experiment
On surface					
(100)	H- > B	0.8[0.25]	*H- > H	1.3 ^b	–
	B- > B'	0.48[0.03]	*H- > H	1.45 ^c	
	*H- > B- > H	0.80	*H- > H	1.46 ^c	
	*H- > B'- > H	1.04			
(110)	LB- > TF	0.11[0.06]	*LB- > LB	1.0 ^b	–
	TF- > TF (same cell)	(0.06)	*LB- > LB	0.96 ^c	
	TF- > TF (neighbor cell)	(0.58)	*LB- > LB	1.21 ^e	
	*TF- > TF- > TF- > A- > TF	(0.58)	*LB- > LB	1.08 ^f	
	*LB- > TF- > TF- > LB	0.62			
(111)	A- > A'	0.56[0.09]	GS- > GS ^{#1}	0.2 ^b	–
	GS- > A	0.40[0.13]	GS- > GS ^{#2}	0.8 ^b	
	GS- > A'	0.82[0.08]	*GS- > GS ^{#1} - > GS ^{#2}	0.8 ^b	
	GS- > A' (neighbor cell)	1.83[1.09]	GS- > GS	(0.93) ^d	
	GS- > A- > GS	0.40	GS- > GS	(1.12) ^e	
	GS- > K- > GS	0.60			
	*GS- > A- > A'- > GS'	0.82			
	*GS- > A- > GS- > A'- > GS'	0.82			
Surface-subsurface					
(100)	H- > OS ₁	1.16[0.35]	H- > OS ₁	1.47[0.3] ^c	–
(110)	A- > LB	0.04[0.18]	LB- > OS ₁	1.44 ^d	1.3±2a*
	A- > OS ₁	(0.99)[0.66]	LB- > OS ₁	1.18[0.56] ^c	
(111)	LB- > A- > OS ₁	1.03	LB- > OS ₁	0.98[0.45] ^f	
	GS- > B	0.44[0.13]	A- > GS	0.17[0.15] ^d	–
	GS- > B'	0.40[0.09]	A- > A	0.45 ^d	
	GS- > B''	0.83[0.03]	A- > B	0.73[0.18] ^d	
	GS- > OS ₁	1.56[0.18]	B- > OS ₁	0.76[0.86] ^d	
	A- > B	0.18[0.09]	A- > B- > OS ₁	1.31 ^d	
	A- > B''	0.60[0.07]	A- > GS	0.43[0.38] ^e	
	A'- > B	0.09[0.47]	A- > N	0.77[0.25] ^e	
	GS- > B- > OS ₁	0.86	A- > N- > A	0.77 ^e	
	GS- > B'- > OS ₁	0.87	A- > GS- > GS	1.17 ^e	
	GS- > B''- > OS ₁	0.87			
Surface-subsurface-surface					
(111)	*GS- > A- > B- > A'- > GS'	0.82	*GS- > A- > GS- > GS	1.17 ^e	–
			*GS- > A- > GS- > GS	0.95 ^d	

^a Wiltner [7], 0.25 ML, method SEQUEST-PBE/GGA. a* XPS measurements.

^b Hong [8], method VASP-GGA. #1 jump via triangle centered in 3rd layer, #2 jump via triangle centered in 2nd layer.

^c Jiang & Carter [10], 0.25 ML carbon coverage, method VASP-PAW/GGA.

^d Xing-wu [12], 0.25 ML carbon coverage, method VASP-PBE/GGA. In (111): GS ≈ d, A ≈ e, (B or B') ≈ S1, OS₁ ≈ S2.

^e Riikonen [6], 0.11 ML carbon coverage, method VASP-PBE/GGA. In (100): H ≈ C-1, B ≈ C-2; In (110): LB ≈ C-1, SB ≈ C-2; In (111): A ≈ C-1, GS ≈ C-2, A' ≈ (saddle of C-2 > C-2), N is octahedral bulk-like beneath A'.

^f Sahputra [44], 0.0625 ML, carbon coverage, method VASP-PBE/PAW.

Table 2

Distance (Å) of C atomic positions to Fe-surface. If positive, the position is under the surface, else it is over the surface. "On surf" or "In subsurf" means that more precise data has not been found but it is known that C is on the surface or into the subsurface.

Site	(100)		(110)		(111)			
	EAM	DFT	Site	EAM	DFT	Site	EAM	DFT
H	-0.27	-0.30 ^a	LB	-0.79	On surf	GS	-0.08	On surf
B	-0.02	On surf	TF	-0.95	On surf	A	-0.08	0.33 ^b
B'	-0.92	On surf	A	-0.26	On surf	A'	-0.61	On surf
						B	0.56	In subsurf
						B'	0.56	In subsurf
						B''	0.73	
OS ₁	1.43	In subsurf	OS ₁	0.91	In subsurf	OS ₁	1.52	In subsurf
OS ₂	2.91	In subsurf	OS ₂	2.09	In subsurf	OS ₂	2.43	In subsurf

^a Jiang & Carter [10].

^b Xing-wu [12].

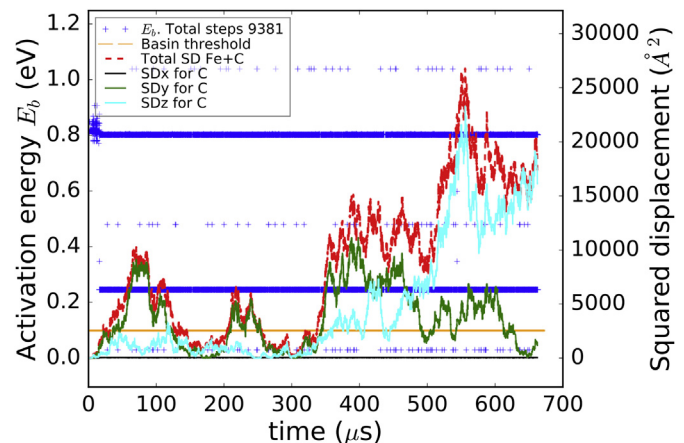


Fig. 3. Energy barriers are shown as points (blue crosses) and square displacement as lines in each direction for C diffusion over the Fe slab cleaved along the (100) surface. Diffusion along the x-axis stops after C arrives at the surface (black flat line). The yellow line is the basin threshold used to handle flickers which was set to 0.1 eV. (For interpretation of the references to colour in this figure legend, the reader is referred to the web version of this article.)

possible paths are via states A to A' or B to A' (jump's energies are summarized in Table 1). Note that the motion via B generates surface-subsurface-surface diffusion pathways. In general, diffusion from unit cell to unit cell is done in two or more steps with an

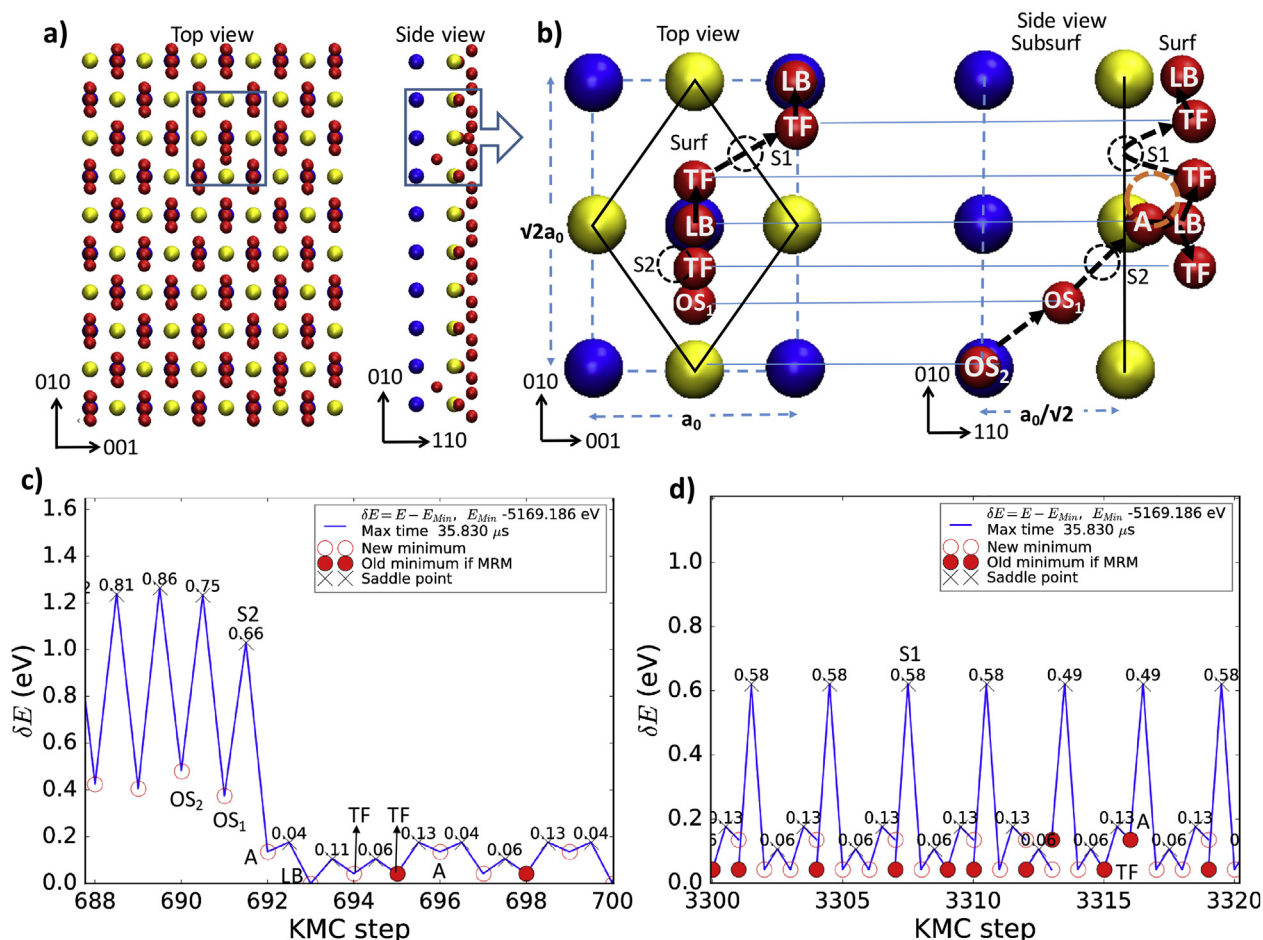


Fig. 4. a) Top and lateral views of the all C positions visited on the Fe (110) surface and subsurface. b) Diffusion mechanisms from bulk to Fe (110) surface and over surface. The red spheres represent the C atom positions on the surface, i.e. the octahedral site OS₁ and OS₂; the ground state long bridge site LB; threefold TF and position A. S1 is a saddle point on the surface at the short bridge SB position and S2 is a saddle point between the subsurface and the surface. The yellow spheres represent Fe atoms at the surface, and the blue ones, Fe atoms at the subsurface; the dashed orange circle represents the Fe new position when C is at the OS₁ site. c) Plot of the energy landscape for jumps from subsurface-to surface and d) energy landscape for jumps on the surface. The energy is measured with respect to the lowest-energy found in the simulation. (For interpretation of the references to colour in this figure legend, the reader is referred to the web version of this article.)

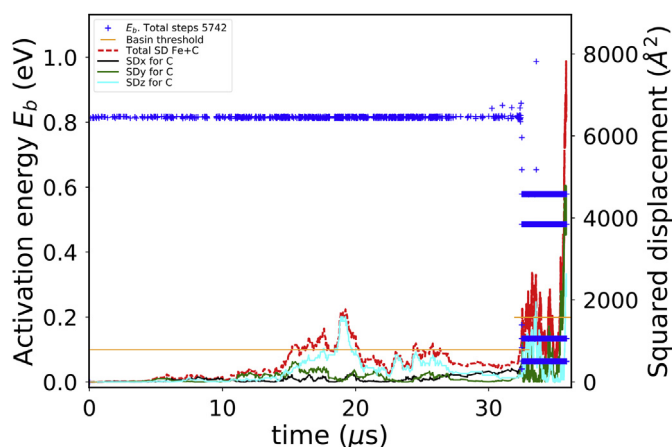


Fig. 5. Energy barriers are shown as points (blue crosses) and square displacement as lines in each direction for C diffusion over the Fe slab cleaved along the (110) surface; predicted using k-ART at 600 K, surface reached at time $t = 32.4$ μ s. The yellow line is the basin threshold used to handle flickers, in bulk set to 0.1 eV and in surface reset to 2 eV. (For interpretation of the references to colour in this figure legend, the reader is referred to the web version of this article.)

effective barrier of 0.82 eV. K-ART also predicts an additional pathway for C diffusion (also not shown) with a 1.83 eV barrier, much too large to be kinetically relevant at 600 K.

3.4. Diffusion from bulk to the (111) surface

In contrast to the other two surfaces, multiple diffusion paths from the bulk to the (111) surface are possible. Fig. 7 shows top and side views of three different pathways, with their respective energies. Starting by the path shown in Fig. 7a,d, we see that the C atom jumps from an octahedral site OS₃ in the fifth layer to a GS on the surface by crossing three consecutive barriers of 0.79 eV, 0.38 eV and 0.1 eV. Similarly for the second path shown in Fig. 7b,e, the C atom jumps from the fifth layer to the surface in four steps with barriers of 0.74 eV, 0.37 eV, 0.1 eV. In the third path, the C jumps in four steps with barriers of 0.67 eV, 0.42 eV, 0.03 eV and 0.09 eV.

Surface to subsurface diffusion can be obtained as before by reverting the pathways shown in Fig. 7d,e,f while analyzing all pathways, even those that have not been visited but are in the event catalog. The dominant jumps here start from the GS to the subsurface positions B, B' and B'' with barriers of 0.44 eV, 0.40 eV and 0.83 eV respectively. The C atom at the locations B, B' and B''

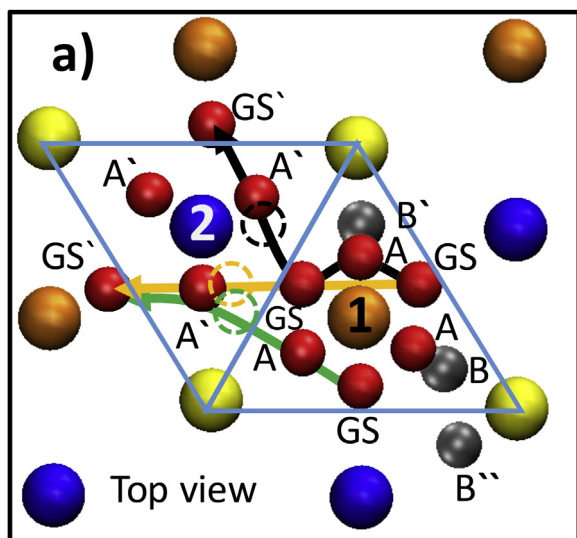


Fig. 6. Minima energy positions found with k-ART on the (111) surface unit cell. The arrows indicate 3 full paths between two ground states: GS to GS'. In red, C atoms at states GS, A, and A' over the surface and gray C atoms at states B, B' and B'' in the subsurface, between the first and second layers. The small dotted circles are some representative saddle points. Yellow represent Fe-atoms in the first layer, blue Fe-atoms in the second layer and orange Fe-atoms in the third layer. (For interpretation of the references to colour in this figure legend, the reader is referred to the web version of this article.)

distorts the unit cell by displacing the Fe atoms to F, F' and F'' positions (Fig. 7a,b,c). These displacements are responsible for the difference of energies between symmetrical points like B and B', both located 0.56 Å beneath the surface (the second and third Fe-layers are at 0.8 Å and 1.57 Å). The point B'', 0.73 Å beneath the surface, appears one step before the C atom jumps from the subsurface to the surface while the B point appears after the C atom is at surface.

Due to presence of a high number of flickering states, in triangle (1), the simulation was limited to following the C atom movement over a limited number of cells, preventing us from extracting a significant diffusion coefficient from the square displacement. From the dominant barriers, however, we can conclude that the (111) surface C diffusion coefficient should be of the same order of magnitude as that in the bulk because the effective barrier is similar.

3.5. Catalog generation for C diffusion from bulk to Fe-surfaces

As explained above, k-ART is a powerful technique that creates an on-the-fly reusable event catalog that provides a full description of the energy landscape at each step during the system's evolution. This full catalog is useful to assess the wealth of barriers and possible events that could be selected at other temperatures. Fig. 8, for example, presents the evolution of the energy landscape as a function of KMC steps as a single C atom migrates from an interstitial site in Fe bulk to the surface. For simplicity, only events with a barrier of 5 eV or less and associated with the C atom are considered, leaving aside, as discussed above, all isolated Fe surface motions. Also, symmetric events are plotted only once in the plots. Plots in Fig. 8 show the distribution of energy barriers (red) and the barrier energy for the selected event (blue). Most of the time, following Boltzmann's distribution, energy barriers within a few electron-volts (around $kT \approx 0.051$ eV at 600 K) of the minimum-energy diffusion mechanism are selected, even though all barriers are included in the catalog.

In the bulk, the event catalog counts four events, associated with equivalent jumps to neighbouring octahedral positions through tetrahedral sites. The event catalog gets richer once the C atom reaches the surface. In Fig. 8a, a total of six different energy barriers are observed for surface and (100) subsurface jumps. The inset detail of Fig. 8a around KMC step 355 shows that cell-cell diffusion is done in two steps crossing barriers of 0.8 eV and 1.03 eV; in agreement with what it is explained in Fig. 2. We observe a similar result for the (110) surface, where k-ART identifies eleven different energy barriers (see detail in Fig. 8b at KMC steps 800–815) but with a maximum of five events per KMC step. These barriers link two local energy minimum configurations that can be occupied by a C atom on the perfect (110) surface and one local minimum in subsurface; as explained in Fig. 4. The third catalog analyzed corresponds to diffusion from bulk to (111) surface. In Fig. 8c, we observe 13 different energy barriers. As before, most of them correspond to flickers and only a few are responsible for diffusion on the surface or to subsurface. A maximum of seven events per step is observed, showing the relative complexity of this surface.

Barriers of more than 1.5 eV are also observed in the (110) and (111) catalogs, these events correspond to a displacement of the C atom beyond a second neighbor or to subsurface and their occurrence probability is several orders of magnitude smaller than the selected events at 600 K. The overall information gained from k-ART, in particular the jumps from the surface to the subsurface combined with our detailed knowledge of the bulk diffusion (which counts only four events), ensures that all relevant pathways between the bulk and the surface for the system studied here are identified. The most relevant of these events are summarized in Table 1 for the three surfaces.

3.6. Comparison to experiments and *ab initio* calculations

In this paper, we have produced an extensive characterization of the energy landscape and diffusion kinetics of C migration in Fe systems with surfaces. Before discussing the physical meaning of the results presented here, however, we first compare with previously available DFT and experimental data.

Table 1 displays the barrier energies computed with k-ART-EAM and *ab initio* results found in the literature. For (100) surface, the minimum B predicted by the EAM approximately corresponds to the saddle geometrical position predicted by DFT. Similarly, absorption and adsorption sites for (110) surface are in good agreement geometrically with the results of DFT [6,10]. In both cases, however, k-ART-EAM predicts a slightly more rugged energy landscape than DFT, with metastable points such as point A, for the (110) surface, that is located below the ground state LB site, and point B' on the (100) surface. This difference could be due to an incomplete sampling or finite size effects with DFT or to imprecisions in the EAM forcefield. More DFT calculations are required clarify this question.

For states common to both approaches, there often remains some energy difference. The 0.58 eV barrier for unit cell to unit cell diffusion on the (100) surface, for instance, is well below that predicted by DFT which predict them to be around 0.96–1.21 eV [6,8,10]. In general, for these surfaces, the EAM potential predicts energy barriers about 30%–40% lower than DFT. However, since most of the experimental results in various materials predict a faster surface than bulk diffusion, often by several orders of magnitude, effective barriers should be lower at the surface, supporting the EAM predictions [43].

On the (111) surface, *ab initio* results predict three stable geometries for adsorption. This leads to several diffusion paths with effective barriers from 0.80 eV to 1.17 eV [6,12]. In contrast, the EAM predicts a total of 6 possible geometries for adsorption: three on the

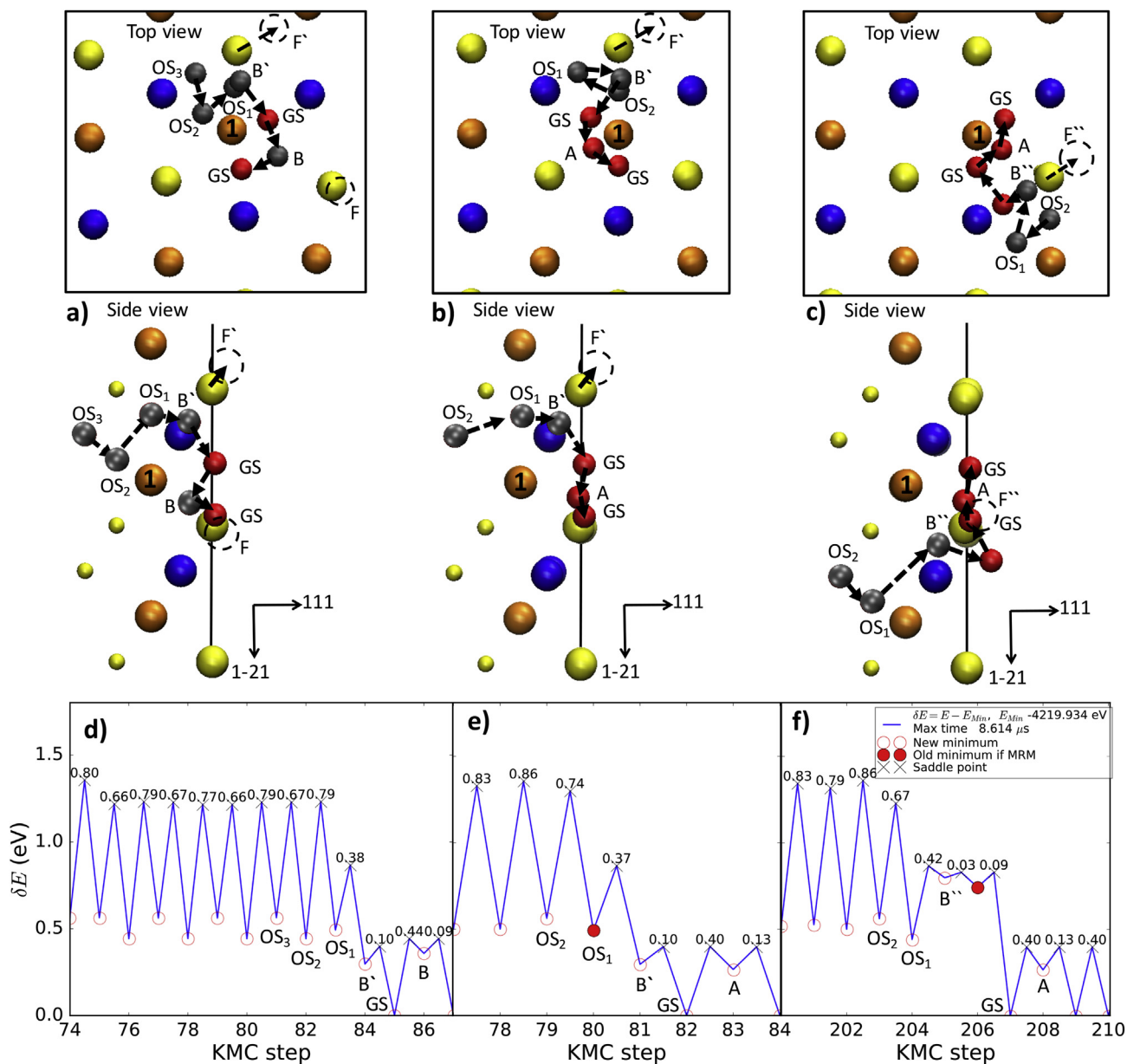


Fig. 7. a), b), c) Top and side views of the 3 different possible pathways for C diffusion from the bulk to the (111) surface. In gray, C positions in the subsurface and in red on surface. F, F' and F'' indicate the corresponding Fe-displacements when C are at B, B' and B''. The small yellow spheres correspond to the rest of the crystal. d), e), f), energies corresponding to the three paths represented in a), b) and c). (For interpretation of the references to colour in this figure legend, the reader is referred to the web version of this article.)

surface plus three more for absorption into the subsurface, thus the number of paths increases. Nevertheless, the effective EAM barrier of 0.82 eV is close to the DFT results. Similarly, geometrical locations of A and GS are approximately in agreement with DFT even though the latter predicts that A is 0.33 Å below the surface while EAM finds A 0.08 Å above the surface. This is why Table 1 presents all the jumps and paths using A as going to the subsurface, as A is a “semi-subsurface” site in DFT. Moreover, the EAM’s GS is not aligned with two Fe atoms at the top surface but is barely pushed into the triangle (1) (compare Figs. 1 and 6). Recent *ab initio* results computed by Riikonen et al. [6] suggest that the lowest energy state is A, with GS 0.05 eV higher in energy, while according to the EAM potential A is 0.27 eV above GS. Finally, DFT identifies A' in the triangle (2) as a saddle point while in k-ART-EAM it is a minimum. The overall pathway and saddle point correspond relatively, well, nevertheless, as A' is 0.74 eV above the GS.

Authors from Ref. [6] predict that even at a low coverage (0.22 ML) of the (110) surface, repulsion between C atoms is strong, but allowing dimer and graphene formation. Besides, they propose that at higher C concentration, C atoms are pushed out to the vacuum, hence reducing the barrier energy. They found a diffusion barrier of 1.21 eV at 0.11 ML which is higher than the 0.96 eV or 1.0 eV proposed in Ref. [10] and ref [7]. A more recent DFT calculation using a much lower coverage of 0.0625 ML [44], predicts a lower barrier of 1.08 eV. Besides, with this same coverage DFT predicts also lower barriers and inverse barriers of 0.98 [0.45] eV to go into the (110) subsurface, compared to 1.18 eV [10], or 1.44 eV [7]. Coverage obviously affects the barrier and makes comparison between our simulations, done at very low coverage and in large systems that decrease size effects, and DFT difficult.

Table 3 presents the energy difference between configurations with the C atom on surface and C atom deep into bulk, $E_{bulk} - E_{GS}$, as

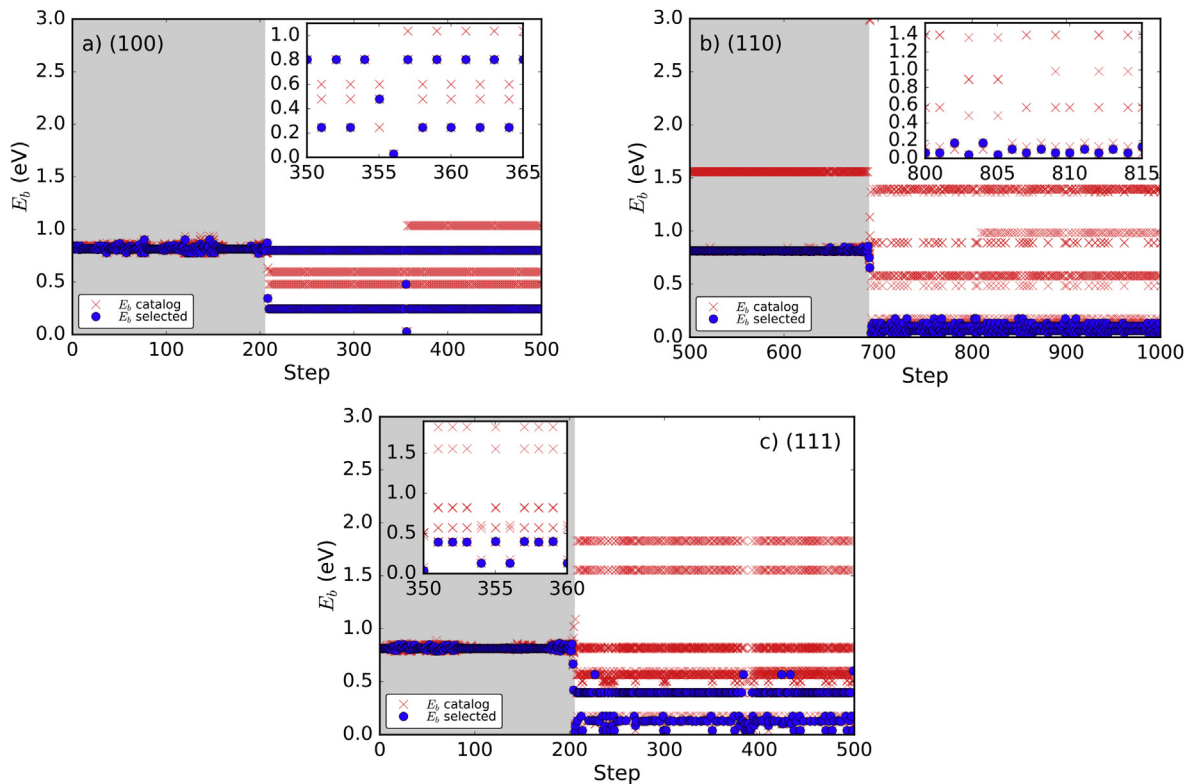


Fig. 8. Energy barriers, E_b , for C-events contained in the catalog at each KMC-step for diffusion from bulk (gray area) to surfaces. Only events involving C are allowed. The red crosses are the full list of energy barriers available at each step and the blue dots are the energy barriers of the selected C-event. Inset figures show zooms of particular intervals when the C atom is on each surface. (For interpretation of the references to colour in this figure legend, the reader is referred to the web version of this article.)

Table 3

Energy difference (in eV) between states of C atom into bulk and on surface, $E_{\text{bulk}} - E_{\text{GS}}$; total effective energy barrier E_{eff} , for C atom to jump from surface to the bulk beyond the third layer; and surface energy E_{surf} (in $\text{meV}/\text{\AA}^2$). Diffusion coefficient in bulk: $D \sim 4.8 \times 10^{-14} \text{ m}^2/\text{s}$.

Surface	$E_{\text{bulk}} - E_{\text{GS}}$		E_{eff}		E_{surf}		D
	EAM	DFT	EAM	DFT	EAM	DFT	
(100)	~0.7	~0.7	~1.6	~1.6	109	140 ^a , 156 ^b	$\sim 2.2 \times 10^{-14}$
(110)	~0.4	~0.4	~1.2	~1.2	101	140 ^a , 152 ^b	$\sim 7.8 \times 10^{-13}$
(111)	~0.5	~0.5	~1.3	~1.3	123	160 ^a , 175 ^b	

^a Riikonen [6].

^b Chakrabarty [19].

well as the effective energy barrier, E_{eff} , required for a C atom to move from the surface to the bulk beyond the third layer as previously described in Figs. 2, 4 and 6 and the surface energies, E_{surf} . In each case the effective barrier E_{eff} , is larger than the diffusion barrier on surface, into subsurface (between first and second layers) and inside the bulk. This clearly indicates that once a first C atom arrives to the surface it should be difficult for it to move into the bulk. The numbers are given with only one digit because E_{bulk} varies according to the exact octahedral point close to surface and that variation emerges as a consequence that the C atom approximates to the surface. E_{surf} also confirms that the (110) surface is the most unstable, while the (110) surface is the most stable. Diffusion coefficients are also summarized in Table 3. We emphasize that these diffusion coefficients are bare approximations and that to have more precise coefficients more KMC steps are required to enhance the statistics.

Comparison of similar events in the (100) and (110) systems evaluated with DFT show good agreement between them. However,

comparisons for the (111) system, both from surface and to subsurface, show large differences between *ab initio* calculations. For example, Riikonen et al. [6] predict a barrier and reverse barrier of 0.43 [0.38] eV at 0.11 ML for events like A- > GS while Xing-wu et al. [12] predict 0.17 [0.15] eV at 0.25 ML; this difference could be a question of coverage. Nevertheless, for all authors the full diffusion path is with an effective barrier around 0.8–1.17 eV, in good agreement with the effective barrier found by k-ART of 0.82 eV. As observed in Table 1, k-ART has found more minima than all the DFT results found in the literature. Computations in DFT are limited to the fact that initial and final minima must be previously known, as the NEB method is used to get the saddle points. In contrast, k-ART explores all possible minima and the uncertainty comes mainly from the empirical potential. The new minima found by k-ART may very well be artifacts from the potential and this needs to be further investigated. Furthermore, we believe that, in general, the large differences between DFT results for similar events are due to the DFT calculation settings, for example the carbon coverage and supercell size used in these calculations. Such problems do not arise in our simulations as k-ART simulations implemented with an empirical potential can be done on large simulation boxes. In addition, Ref [6]'s predicts a second diffusion path via the subsurface with a lower energy barrier of 0.48 eV and Ref [12]'s predicts another subsurface pathway with a 0.73 eV barrier, after careful analysis of the symmetries, we believe that these two barriers are associated with flickering oscillations rather than to jumps leading to real diffusion.

Experimental results for the migration energies on any of the surfaces are not available to our knowledge. Only one paper reports an energy barrier associated to surface to (110) subsurface diffusion based on the XPS technique [7]. This experimental energy barrier is consistent with both DFT and our results.

Finally, while the mechanisms and the general conclusions for the three systems should hold generally, note that the surface energies predicted by the EAM potential differ from that obtained with DFT by up to ~40%, generally from the low side. This means that the real overall insertion rate could be higher than found here.

4. Discussion

Accessing large time scale and system sizes, k-ART simulations presented here provide a detailed characterization of the C kinetics between Fe surfaces and bulk and the associated energy landscapes, showing a relatively complex picture even for the simplest of surfaces. This picture is well characterized with k-ART, since the catalog is updated and expended at every step, as new topologies are explored.

For Fe(100), for example, two dominant pathways are found for C surface diffusion, one going slightly above the surface, with a net barrier of 1.04 eV, one slightly below, preferred with a 0.80 eV barrier. While additional pathways also exist in subsurface, they are unlikely since interstitial positions inside the Fe are much costlier than at the surface and the asymmetric barriers favor expulsion of the impurity.

Fe(110) is slightly rougher, and C diffusion in a three-step process, crossing first two low barriers, before jumping over a 0.58 eV barrier, that dominates the kinetics. While diffusion into the bulk is easier from this surface, with a net barrier of about 1.25 eV compared with 1.63 eV for (100), even at 600 K, this path is rarely sampled.

For both of these surfaces, we find a single pathway for insertion, as all sites below surface have the same symmetry. This is not the case for Fe(111) which shows a much richer energy landscape due to its lower density packing. Surface diffusion can take place through six different pathways, with one going fully through subsurface. In spite of this richness, surface diffusion kinetics is comparable to Fe(100), with minimum effective barriers of 0.82 eV.

As interesting, however, is the existence of three different relevant insertion pathways from this surface associated with different entry points. While, the net effective barrier to the bulk is almost identical for these three mechanisms, their existence might affect C diffusion in the presence of impurities, for example.

As indicated in the results section, we focus our discussion on the most probable mechanisms. Other C diffusion mechanisms, with barriers between 1.3 and 1.8 eV are also identified with k-ART. Since these are much rarer, however, we did not discuss them here in details, but the presence of strain, defects or other impurities could lower the barrier and make them relevant.

Our simulations also suggest that crystalline Fe plays little role in C diffusion. Indeed, while pure Fe diffusion was not allowed, Fe situated in the vicinity of the C atom were allowed to partake into events and even dominate the move. Yet, such events involve high barriers and do not contribute to C diffusion suggesting that for a perfect crystal, C diffusion takes place mostly without disturbing the lattice, even at surfaces.

As discussed in the previous section, results obtained here using EAM potential are in general agreement with experiments and DFT calculations. Using larger cells, to decrease finite-size effects, and offering an extensive characterization of the energy landscape, however, these simulations offer a more complete picture of C diffusion at the surface and into the bulk and demonstrate the need for defects and other impurities to facilitate C insertion into Fe.

5. Conclusion

A characterization of the C atom diffusion from the bulk to the three crystalline bcc iron surfaces – (100), (110) and (111) – has

been done using k-ART implemented with an EAM potential. The more complete energy landscape generated here and obtained with simulations that reached several milliseconds allows us to identify new mechanisms for C diffusion from bulk to the surfaces and on the surfaces.

The C most stable configurations at the three Fe-surfaces are in good agreement with the predictions of DFT even though barrier energies differ by up to 40%. The agreement is even better for the energy barriers corresponding to surface to subsurface diffusion with a difference about 20% or less compared to DFT. This difference means that our simulations tend to predict lower insertion rates and favor surface diffusion, in agreement with experimental observations for the (110) surface, suggesting that DFT's results might suffer from possible biases of DFT, linked in particular to finite size effects, that lead to incorrect barriers. Moreover, our approach provides a detailed and reliable representation of the diffusion paths from surface to subsurface, including rare pathways that are orders of magnitude less likely to occur in pure Fe than the dominant ones. This allows us to conclude that, at 600 K, (100) and (110) will show unique diffusion paths while (111) should present more complex, multistep, multipathway diffusion mechanisms.

The effective barrier E_{eff} , of ~1.6, ~1.2 and ~1.3 predicted by k-ART for diffusion from surface to the bulk inside are larger than (1) the diffusion barrier on surfaces, (2) into subsurface and (3), inside the bulk, which clearly indicates that once a first C atom arrives to the surface it should be difficult for it to move into the bulk. By providing an extensive characterization of the C–Fe landscape, these results also indicate that further study in the presence of defects and additional impurities are therefore needed to establish C insertion mechanism.

Overall, these results provide a much deeper understanding of C diffusion and insertion in bulk bcc iron. They also demonstrate the need for unbiased and extensive approaches for sampling the energy landscape and diffusion mechanisms of even apparently simple systems such as a single C in iron. A need that is even more important when we move to the more complex environments, with defects and impurities, that seem necessary to see C diffusing into bulk Fe.

Acknowledgements

This work is supported by the Qatar National Research Fund (QNRF) through the National Priorities Research Program (NPRP 6-863-2-355). This work was also supported in part by grants from the Natural Sciences and Engineering Research Council of Canada (NSERC). We are grateful to Calcul Québec/Compute Canada (CQ/CC) for generous allocations of computer resources. The k-ART package is available for distribution by contacting the authors.

References

- [1] G.Y. Lai, High-temperature Corrosion and Materials Applications, ASM International, 2007. Chapter 5, Carburization and Metal dusting, page 97. ISBN 1615030557, 9781615030552, Length 461 pages.
- [2] R.B. Anderson, The Fischer-tropsch Synthesis, Academic Press, New York, 1984.
- [3] P. Yvon, F. Carré, Structural materials challenges for advanced reactor systems, J. Nucl. Mater. 385 (2009) 217.
- [4] N.A. Vinogradov, A.A. Zakharov, V. Kocovski, J. Ruzs, K.A. Simonov, O. Eriksson, A. Mikkelsen, E. Lundgren, A.S. Vinogradov, N. Mårtensson, A.B. Preobrajenski, Formation and structure of graphene waves on Fe(110), Phys. Rev. Lett. 109 (2012) 026101.
- [5] A.J. Page, F. Ding, S. Irlé, K. Morokuma, Insights into carbon nanotube and graphene formation mechanisms from molecular simulations: a review, Rep. Prog. Phys. 78 (2015) 036501.
- [6] S. Riikonen, A.V. Krashennnikov, R.M. Nieminen, Submonolayers of carbon on α -Fe facets: an ab initio study, Phys. Rev. B 82 (2010) 125459.
- [7] A. Wiltner, Ch. Linsmeier, T. Jacob, Carbon reaction and diffusion on Ni(111), Ni(100), and Fe(110): kinetic parameters from x-ray photoelectron

- spectroscopy and density functional theory analysis, *J. Chem. Phys.* 129 (2008) 084704.
- [8] S. Hong, Surface energy anisotropy of iron surfaces by carbon adsorption, *Curr. Appl. Phys.* 3 (2003) 457.
- [9] X.W. Liu, C.F. Huo, Y.W. Li, J. Wang, H. Jiao, Energetics of Carbon deposition on Fe(100) and Fe(110) surfaces and subsurfaces, *Surf. Sci.* 606 (2012) 733.
- [10] D.E. Jiang, E.A. Carter, Carbon atom adsorption on and diffusion into Fe(110) and Fe(100) from first principles, *Phys. Rev. B* 71 (2005) 045402.
- [11] D.J. Young, J. Zhang, Understanding metal dusting mechanisms, *ECS Trans.* 16 (3) (2009).
- [12] L. Xing-wu, L. Yong-wang, W. Jian-guo, H. Chun-fang, Energetics of Carbon deposition on Fe(100) and Fe(110) surfaces and subsurfaces, *J. Fuel Chem. Technol.* 40 (2012) 202.
- [13] H.J. Grabke, G. Tauber, H. Viehhaus, Equilibrium surface segregation of carbon on iron (100) faces, *Scr. Metall.* 9 (1975) 1181.
- [14] H.J. Grabke, G. Tauber, H. Viehhaus, Equilibrium surface segregation of dissolved nonmetal atoms on iron(100) faces, *Surf. Sci.* 63 (1977) 377.
- [15] W. Arabczyk, F. Storbeck, H.J. Müssig, Electron spectroscopy studies on carbon segregation from a mono-crystalline α -Fe(111) specimen, *Appl. Surf. Sci.* 65/66 (1993) 94.
- [16] W. Arabczyk, D. Moszyński, U. Narkiewicz, The comparison of the different adsorption states of non-metals on the iron surface, *Vacuum* 54 (1999) 3.
- [17] G. Henkelman, H. Jonsson, A climbing image nudged elastic band method for finding saddle points and minimum energy paths, *J. Chem. Phys.* 113 (2000) 9901.
- [18] G. Henkelman, H. Jonsson, Improved tangent estimate in the nudged elastic band method for finding minimum energy paths and saddle points, *J. Chem. Phys.* 113 (2000) 9978.
- [19] A. Chakrabarty, O. Bouhali, N. Mousseau, C. Becquart, F. El-Mellouhi, Insights on finite size effects in ab initio study of CO adsorption and dissociation on Fe 110 surface, *J. Appl. Phys.* 120 (2016) 055301.
- [20] A. Chakrabarty, O. Bouhali, N. Mousseau, C. Becquart, F. El-Mellouhi, Influence of surface vacancy defects on the carburisation of Fe 110 surface by carbon monoxide, *J. Chem. Phys.* 145 (2016) 044710.
- [21] N. Mousseau, L.K. Béland, P. Brommer, F. El-Mellouhi, J.F. Joly, G.K. N'Tsouaglo, O. Restrepo, M. Trochet, Following atomistic kinetics on experimental time-scales with the kinetic Activation–Relaxation Technique, *Comput. Mater. Sci.* 100 (2015) 111.
- [22] P. Brommer, N. Mousseau, Comment on “mechanism of void nucleation and growth in bcc Fe: atomistic simulations at experimental time scales, *Phys. Rev. Lett.* 108 (2012) 219601.
- [23] A.F. Voter, Classically exact overlayer dynamics: diffusion of rhodium clusters on Rh(100), *Phys. Rev. B* 34 (1986) 6819.
- [24] A. Voter, Introduction to the kinetic monte carlo method, *Radiat. Eff. Solids* 235 (2007) 1.
- [25] C. Becquart, J. Raulot, G. Bencteux, C. Domain, M. Perez, S. Garruchet, H. Nguyen, Atomistic modeling of an Fe system with a small concentration of C, *Comput. Mater. Sci.* 40 (1) (2007) 119.
- [26] R. Veiga, C. Becquart, M. Perez, Comments on “Atomistic modeling of an Fe system with a small concentration of C”, *Comput. Mater. Sci.* 82 (2014) 118.
- [27] F. El-Mellouhi, N. Mousseau, L.J. Lewis, Kinetic activation-relaxation technique: an off-lattice self-learning kinetic Monte Carlo algorithm, *Phys. Rev. B* 78 (2008) 153202.
- [28] L.K. Béland, P. Brommer, F. El-Mellouhi, J.F. Joly, N. Mousseau, Kinetic activation-relaxation technique, *Phys. Rev. E* 84 046704 (2011).
- [29] B.D. McKay, Practical graph isomorphism, *Congr. Numer.* 30 (1981) 45.
- [30] B.D. McKay, A. Piperno, Practical graph isomorphism, II, *J. Symb. Comput.* 60 (2014) 94.
- [31] G. Barkema, N. Mousseau, Event-based relaxation of continuous disordered systems, *Phys. Rev. Lett.* 77 (1996) 4358.
- [32] R. Malek, N. Mousseau, Dynamics of Lennard–Jones clusters: a characterization of the activation-relaxation technique, *Phys. Rev. E* 62 (2000) 7723.
- [33] E. Machado-Charry, L.K. Béland, D. Caliste, L. Genovese, T. Deutsch, N. Mousseau, P. Pochet, Optimized energy landscape exploration using the ab initio based activation-relaxation technique, *J. Chem. Phys.* 135 (2011) 034102.
- [34] B. Puchala, M.L. Falk, K. Garikipati, An energy basin finding algorithm for kinetic Monte Carlo acceleration, *J. Chem. Phys.* 132 (2010) 134104.
- [35] M. Mendelev, S. Han, D. Srolovitz, G. Ackland, D. Sun, M. Asta, Development of new interatomic potentials appropriate for crystalline and liquid iron, *Philos. Mag.* 83 (2003) 3977.
- [36] C. Domain, C.S. Becquart, Ab initio study of foreign interstitial atom (C, N) interactions with intrinsic point defects in α -Fe, *J. Phys. Rev. B* 69 (2004) 144112.
- [37] R.G.A. Veiga, M. Perez, C.S. Becquart, C. Domain, Atomistic modeling of carbon Cottrell atmospheres in bcc iron, *J. Phys. Condens. Matter* 25 (2013) 025401.
- [38] N. Gunkelmann, H. Ledbetter, H.M. Urbassek, Experimental and atomistic study of the elastic properties of α' Fe–C martensite, *Acta Mater.* 60 (12) (2012) 4901.
- [39] R. Veiga, M. Perez, C. Becquart, E. Clouet, C. Domain, Comparison of atomistic and elasticity approaches for carbon diffusion near line defects in α -iron, *Acta Mater.* 59 (2011) 6963.
- [40] S. Plimpton, Fast parallel algorithms for short-range molecular dynamics, *J. Comput. Phys.* 117 (1995) 1.
- [41] Lammmps web site. <http://lammmps.sandia.gov/index.html>.
- [42] O.A. Restrepo, N. Mousseau, F. El-Mellouhi, O. Bouhali, M. Trochet, C.S. Becquart, Diffusion properties of Fe–C systems studied by using kinetic activation–relaxation technique, *Comput. Mater. Sci.* 112 (2016) 96.
- [43] Helmut Mehrer, *Diffusion in Solids Fundamentals, Methods, Materials, Diffusion-controlled Processes*, Springer Berlin Heidelberg, New York, 2007.
- [44] I.H. Sahputra, A. Chakrabarty, O. Restrepo, O. Bouhali, N. Mousseau, C.S. Becquart, F. El Mellouhi, Carbon adsorption on and diffusion through the Fe(110) surface and in bulk: developing a new strategy for the use of empirical potentials in complex material set-ups, *Phys. Status Solidi B* (2016) 1–11.